

## EVALUATING THE MECHANICAL PROPERTIES WITHIN THE TRANSITION REGION OF MULTI-MATERIAL LARGE-FORMAT EXTRUSION ADDITIVE MANUFACTURING

J. Brackett<sup>1</sup>, A. Defilippis<sup>2</sup>, T. Smith<sup>3</sup>, A. Hassen<sup>3</sup>, V. Kunc<sup>3</sup>, and C. Duty<sup>2,3</sup>

<sup>1</sup>Bredesen Center for Interdisciplinary Research, University of Tennessee – Knoxville, TN

<sup>2</sup>Mechanical, Aerospace, and Biomedical Engineering, University of Tennessee – Knoxville, TN

<sup>3</sup>Manufacturing Science Division, Oak Ridge National Laboratory, Oak Ridge, TN

### **Abstract**

Recent developments in Large-Format Additive Manufacturing (LFAM) have enabled in-situ material changes and production of graded Multi-Material (MM) structures. The Big Area Additive Manufacturing (BAAM) system utilizes a dual-hopper configuration to feed different materials into a screw-based extruder which results in a blended material transition rather than a discrete material boundary, avoiding associated delamination issues. While this system enables site-specific material deposition at a large scale, the mechanical performance within the transition region needs to be evaluated to determine the impact on end-part performance. Additionally, the transition region can exhibit incomplete mixing, which could further influence mechanical performance. This study investigates the change in mechanical properties throughout the transition region using dynamic mechanical analysis and tensile testing of printed samples. Optical microscopy of the internal microstructure of the printed beads was also utilized to determine the influence of material blending within the transition on mechanical performance.

### **1. Introduction**

Additive Manufacturing (AM) provides a unique ability to construct complex geometries [1, 2], which can be further leveraged with the implementation of multiple materials in the printing process. Development of Multi-Material Additive Manufacturing (MMAM) has recently seen significant interest [3-8], largely due to the ability to create complex structures exhibiting site-specific properties. MMAM systems must be capable of utilizing more than one material without pre-mixing, pre-compositing, or non-AM post processing treatments [9]. Although there are MMAM systems available for several different types of AM processes, most encounter the same challenge of bonding dissimilar materials during the printing process. These sections of the printed parts are often structural weak points vulnerable to delamination. Vu et al. observed this behavior in T-Peel geometry samples printed with a Stratasys PolyJet Connex 350, noting that fractures occurred more often in the material interfaces. However, aligning interfaces perpendicular to build direction provided increased resistance to fracture at the interface [5, 6]. Similar behavior has also been observed in Fused Filament Fabrication (FFF) systems. Brischetto et al. observed delamination failure at the interfaces in acrylonitrile butadiene styrene (ABS) and polylactic acid (PLA) sandwich structures [3]. As with the PolyJet system, Kim et al. found that placing interfaces perpendicular to build direction increased resistance compared to interfaces parallel to build direction, but the interfaces remained the most vulnerable to failure [10]. Similarly, Roger and Krawczak demonstrated that placing the interface in multiple z-direction planes increases delamination resistance but still underperforms a single-material counterpart [11].

One method of mitigating the impact of discrete boundaries between dissimilar materials is the usage of stepwise Functionally Graded Material (FGM) construction. This method uses discrete steps of intermediate composition between two materials to improve interfacial bonding and create a property gradient. Vu et al. implemented a stepwise FGM core in T-Peel testing and observed an increased resistance to delamination compared to the previous single-material cores [6]. A similar approach was used in the construction of a functional robot shell to vary the elastic modulus from 1 MPa to 1 GPa, providing a balance between flexibility and rigidity that outperformed single-material designs [4]. Some studies have demonstrated the benefits of continuous FGMs, or those with a continuous compositional change and no discrete boundaries, over the stepwise counterparts, especially in bioinspired and biopolymer composite applications [12, 13]. The success of these methods has seen FGMs used in the creation of orthopedic implants [14, 15]. Extensive reviews cover additional unique applications of FGMs using MMAM with a variety of processes and materials [16-18]. Regardless of the situation, FGMs have been used to solve processing issues between otherwise incompatible materials.

Recent work on Cincinnati Incorporated's Big Area Additive Manufacturing (BAAM) system has included the addition of an automated dual-hopper that enables in-situ material changes by rocking the attachment to select which of the two hoppers is currently supplying material to the extrusion system [8]. Initiating a step-change from Material A to B during extrusion creates a graded region of mixed material composition termed the Transition Zone. As shown in Figure 1, characterization of the progression from Material A to Material B has further defined three stages: an initial Purge Zone of Material A that was already present in the extrusion system followed by the Transition Zone before culminating in a Steady-State extrusion of Material B [19-21]. Further investigation indicated that changes in processing conditions such as rotational speed and screw geometry can affect this transition behavior [21]. In addition to understanding how the material composition changes after switching materials with this system, there is also a need to characterize the mechanical performance. This study investigates the change in mechanical response across the transition region and compares it to observed changes in material composition.

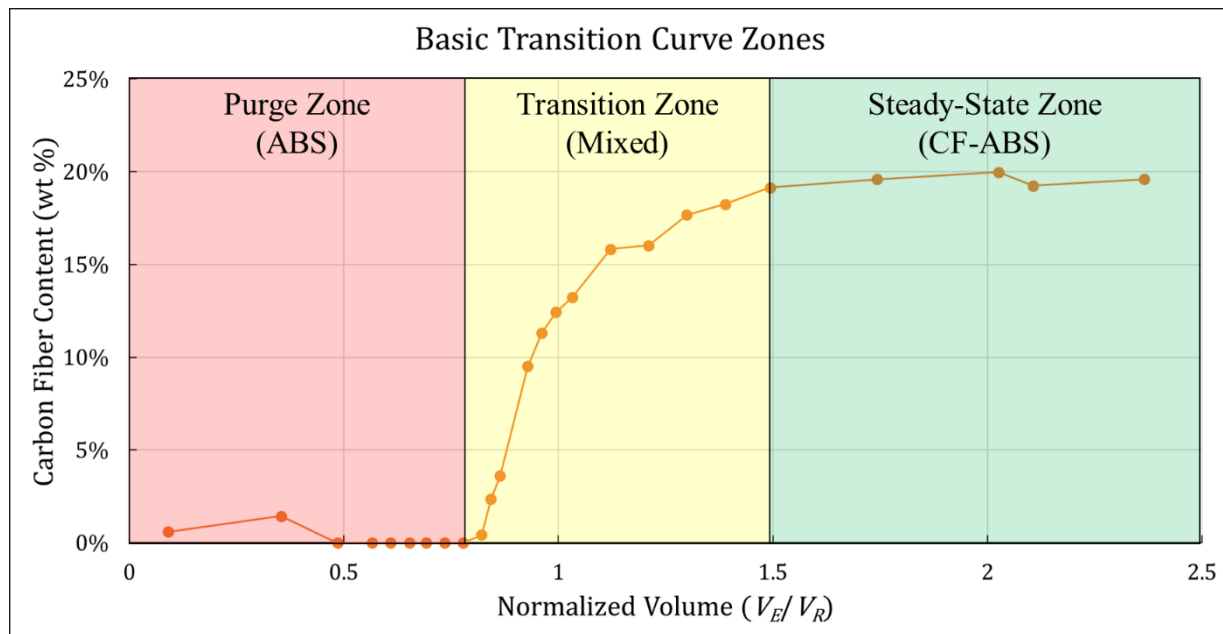


**Figure 1:** A previously characterized material transition showing the purge (red), transition (yellow) and steady-state (green) zone boundaries marked with semi-transparent overlays.

## 2. Experimental

Two structures were printed using the dual-hopper system such that each structure represented a complete material transition: 20 wt % carbon fiber-filled ABS to ABS (CF to ABS) and ABS to 20 wt % carbon fiber-filled ABS (ABS to CF). Dynamic Mechanical Analysis (DMA) and Ultrasonic Assisted Acid Digestion (UAAD) were used to obtain storage moduli and material compositions, respectively. These two properties were then plotted as a function of a normalized extruded volume to compare changes in behavior with material composition.

### 2.1 Sample Printing

All samples were printed using the BAAM and the novel dual-hopper attachment at ORNL's Manufacturing Demonstration Facility. Techmer Engineered Solutions supplied two grades of ABS in pelletized form: a neat ABS (HIFILL ABS 1512 3DP) and a 20 wt % CF/ABS (ELECTRAFIL ABS 1501 3DP). Prior to printing, each material was dried at 80 °C for at least four hours. The print used a nozzle diameter of 10 mm (0.4 in) and bead dimensions of 5 mm (0.2 in) by 14 mm (0.55 in). Thermal conditions were kept constant with a bed temperature of 100 °C and a melt temperature of 250 °C. All samples were printed using a standard mixing screw geometry and screw speed of 300 RPM.

Figure 2A shows the programmed print path, which isolated each transition direction to a single structure to simplify analysis. Using a zero percent infill, the print path was intended to create a block U-shaped, single-bead wall with the shown dimensions, which can be seen in Figure 2B. For both the diagram and the image, the red dot represents the point where the dual-hopper switches material and changes transition direction, and the arrows illustrate the travel direction of

the print head. The final products were 27 layers (approximately 14 mm) tall to provide adequate room for sample creation in both the x- and z-directions.

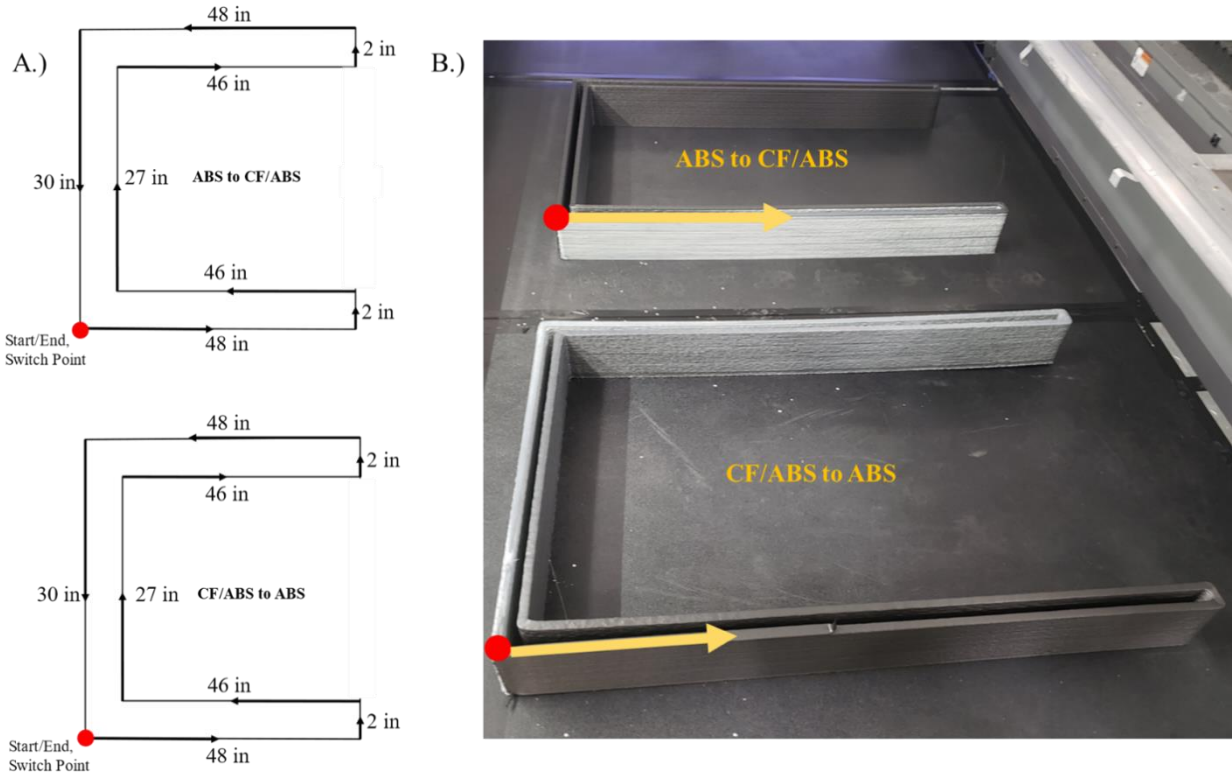


**Figure 2:** A.) A schematic showing the print path and dimensions. Each structure shows transition direction; red dots mark both the start and end of a transition print and where material switches. B.) Printed specimens on bed.

## 2.2 Sample Machining

Using a bandsaw, the completed prints in Figure 2B were first sectioned into 96.5 mm (3.8 in) long plates and then each plate was split in half perpendicular to the print direction to obtain two sides (A and B) of the same composition. This allowed for additional samples from the same composition range, enabling a more thorough and reliable mechanical analysis. As shown in Figure 3A, all plates were milled flat, and four samples in each direction (x and z) per plate were extracted using water jet cutting, resulting in a total of 16 possible samples for a print location. Samples adhered to dimensional specifications found in ASTM D5023 [22]. Due to constraints imposed by the testing equipment (40 mm span), sample thickness was adjusted to remain in tolerance. Any samples damaged during the machining process or that did not fall within specified tolerances were discarded. Sample location was tracked using the travel distance of the extruder from the material switch origin (See Figure 2A). For data analysis, sample sets were identified by the travel distance at the center of the x-direction samples, as shown in Figure 3B. distance traveled by the extruder since changing material, and sample sets were defined by the range covered, i.e., the travel distances at each end of the x-direction samples. For data analysis and plotting, the center of these two points was used to identify the location of a set along the print.

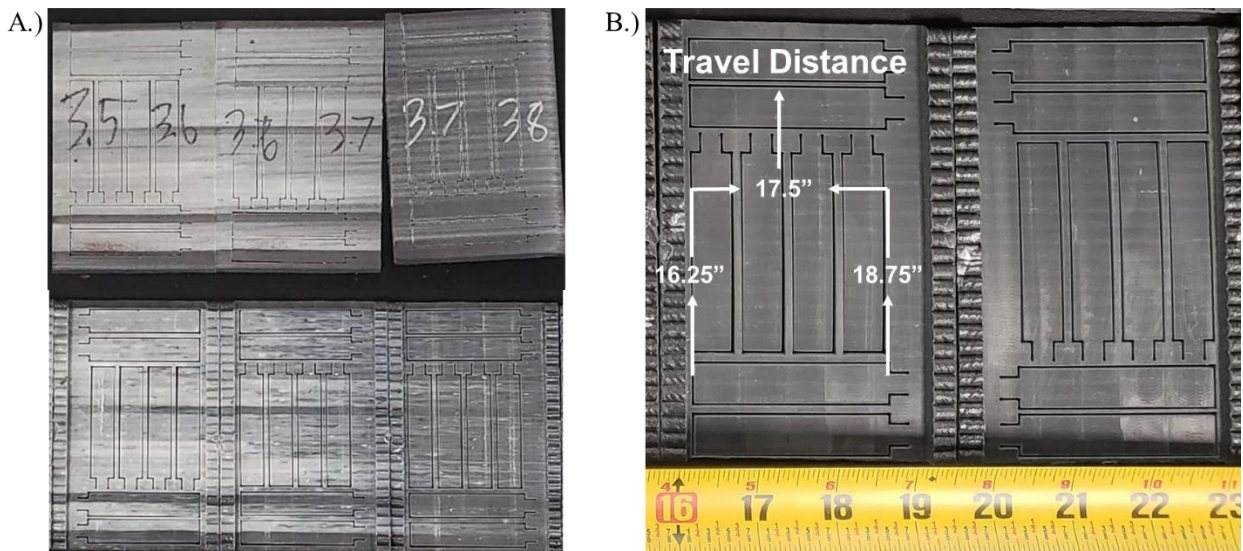


**Figure 3:** A) Example of the “A” (top) and “B” (bottom) and side plates consisting of the same composition, and B.) A schematic showing how travel distance was identified for each sample set.

### 2.3 DMA Testing Procedure

DMA was conducted using a TA Instruments Discovery Hybrid Rheometer (DHR) in “Three-Point Bend DMA” mode, which mimics a flexural test arrangement. The DHR will perform an operator-programmed frequency sweep and calculate the material response to an increasing rate of deformation while holding constant or varying amplitude and temperature. While testing determines the storage modulus ( $G'$ ), loss modulus ( $G''$ ), and phase angle ( $\delta$ ), only the storage moduli were reported for the purposes of this study. Focusing on  $G'$  values provided a simplified method for comparing changes in material composition to measured elasticity.

The chosen procedure ran a logarithmic sweep over a standard range of 0.1 to 10 Hz, collecting four points per decade. Following ASTM D5023, the strain amplitude was set to 0.01 %, and the initial static force was set at 1 N. Testing was conducted using the largest test frame (40 mm span) compatible with the DHR. The average width and thickness of each sample was manually measured and input into the program prior to test start.

For the CF to ABS transition, a significant number of samples were damaged during machining. As a result, some data points were not reported with standard deviations to avoid misrepresenting those points as having the required number of tests to report an accurate average. For all other sample sets, at least four samples were tested to obtain an average.

### 2.4 Measuring Material Composition

Material composition was obtained at numerous locations in the printed sample, with an increased frequency during transition, to provide context for any observed changes in mechanical response. Since this study used one neat and one fiber-filled material, composition was tracked through changes in fiber content. Weight percent carbon fiber (wt % CF) was found using Ultrasonic-Assisted Acid Digestion (UAAD), which has proven to be a reliable method for

accurately characterizing sample composition [19, 20]. As noted, samples were labelled according to distance travelled by the extruder since the material switch. Since the locations of DMA samples did not exactly match that of the available composition data, the measured wt % CF values were interpolated to find the approximate wt % CF of each DMA sample set. The resulting fiber content was used to calculate a corresponding flow rate and improve extruded volume calculations for DMA samples.

## 2.5 Extruded, Residual, and Normalized Volume

Both material composition and G' were plotted as a function of volume and compared to determine how changes in material composition affected elasticity. To accurately calculate the volume extruded,  $V_E$ , at specific points within the print, the measured volumetric flow rate,  $Q$ , was multiplied by the distance traveled by the extruder,  $d$ , and divided by known travel speed,  $t_s$ , as shown in Equation 1.

$$V_E = \frac{Q \times d}{t_s} \quad (1)$$

This approach considers any differences between transition directions caused by a change in volumetric flow rate as material changes while also avoiding a reliance on a uniform bead cross-section to calculate volume. To better relate extruded volume to the BAAM,  $V_E$  is normalized by the standard material volume that occupies the space between the material switch point and the nozzle exit, i.e. the residual volume,  $V_R$ . With normalized volume,  $V_N$ , the extruded volume is directly related to the remaining Material A in the system after switching to Material B, which provides clear and meaningful boundaries for observed transition behavior. All transitions should begin before “1”  $V_N$  and have roughly equal volumes of Material A on each side of “1”. Transition comparisons can thereby focus on the shape of the curve around  $V_N = 1$  and meaningfully represent the dispersion of the discrete material boundary caused by the step-change in material. Furthermore, utilizing both Equations 1 and 2 allows for transitions printed under different condition to be compared.

$$V_N = \frac{V_E}{V_R} \quad (2)$$

## 2.5 Plotting against $V_N$

Both carbon fiber content and G' were plotted as a function of normalized volume. Using a separate y-axis for each data type better visualized the relationship between material composition and G', which aided in discussing the impact of changing material composition on storage modulus. Results for z-direction testing were plotted first alone then together with x-direction data to illustrate that observed trends hold regardless of testing direction and then show that the true impact was negligible compared to changes seen in x-direction testing.

### **3. Results and Discussion**

#### **3.1 Effect of Frequency on G'**

Three-point bend DMA data was collected for four distinct experimental groups: x- and z-directions for both ABS to CF and CF to ABS transitions. Since the programmed frequency sweep calculates  $G'$  at each frequency studied, there was a need to verify that using data from a single frequency would not compromise analysis. Thus, the storage moduli calculated at a high (5.62 Hz) and a low frequency (0.18 Hz) relative to the range covered by the frequency sweep were plotted as two separate trends. The average  $G'$  and standard deviation of ABS to CF x-direction samples for each frequency can be seen in Figure 4 as a function of normalized volume. While the difference between high and low frequency  $G'$  increased in the CF/ABS region, the differences were minimal, and values remained well within the standard deviation. More importantly, the same trend can be seen for both data sets: a plateau in the ABS region followed by a gradual increase during the material change that culminates in a second plateau in the CF/ABS region. This behavior was consistent for the three remaining experimental conditions, validating expectations that data from a single frequency within the LVR could be representative of general trends in mechanical response. To more closely mimic traditional flexural testing by maximizing the elastic components, high frequency results acted as representative data.

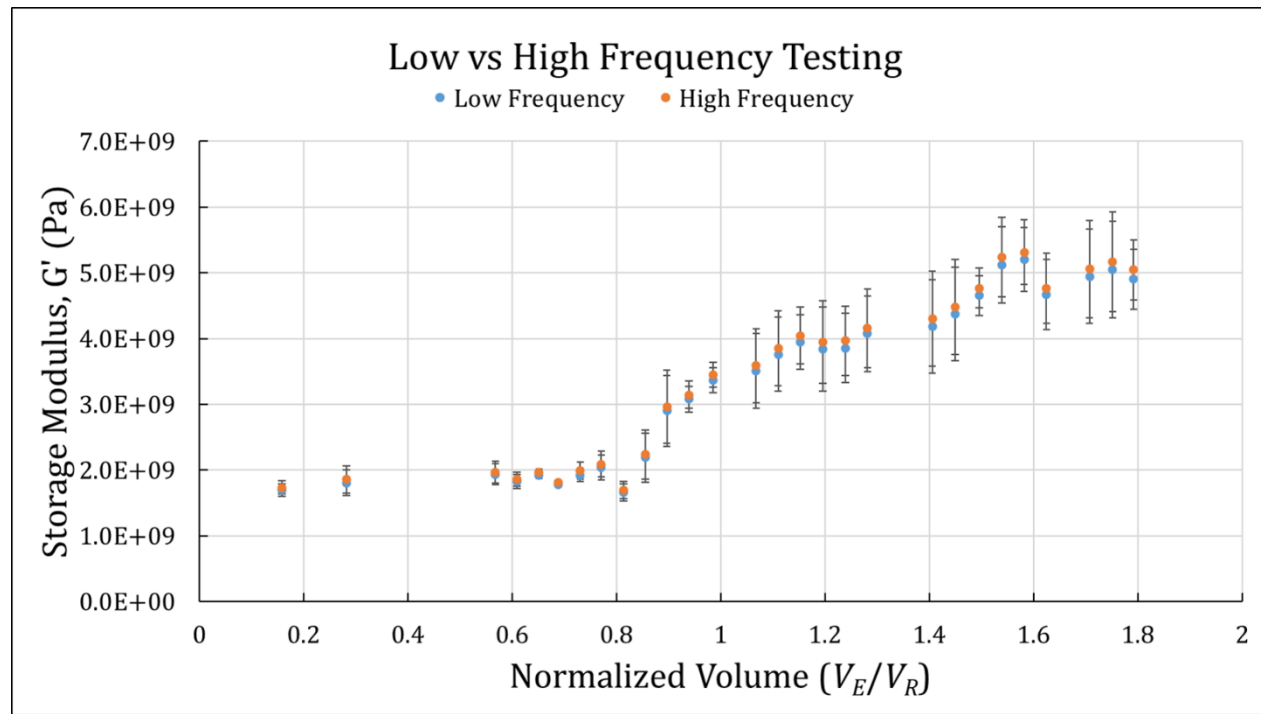


**Figure 4:** X-direction storage moduli at the chosen high and low frequencies against board position for ABS to CF/ABS.

### 3.2 G' and Material Composition

Figure 5 shows both  $G'$  and material composition against the normalized volume. As expected, both curves begin prior to and end after  $V_N = 1$ , and  $G'$  measurements exhibited a lower-value plateau in the ABS region (purge zone) and a higher-value plateau in the CF/ABS region (steady-state zone). In the transition zone,  $G'$  increased with increasing fiber content. Specifically, any change in material composition had an immediate effect on the calculated storage modulus rather than being a lagging or forward indicator. The increase in  $G'$  as composition changed across the transition zone would be expected from a mixed material region, indicating that mixing during extrusion was sufficient to prevent degraded material properties. Further, the lack of any visible stair-stepping effect suggests that there were no thresholds in material composition that need to be overcome to see a change in mechanical behavior. As can be seen in Figure 6, z-direction samples exhibited similar behavior as the x-direction samples. This consistent behavior suggests that the transition zone storage modulus can therefore be approximated using a simple rule of mixtures approach based on material composition. Figures 5 and 6 also indicated that standard deviation was influenced by two separate phenomena: carbon fiber content and zone changes. For each data set, increasing carbon fiber content led to an increase in standard deviation, and both the onset and end of the transition zone caused spikes in standard deviation. While wt % CF could cause variance through inconsistencies in dispersion and orientation, the spikes when switching zones are most likely due to poor mixing caused by the change in feedstock type and shape.

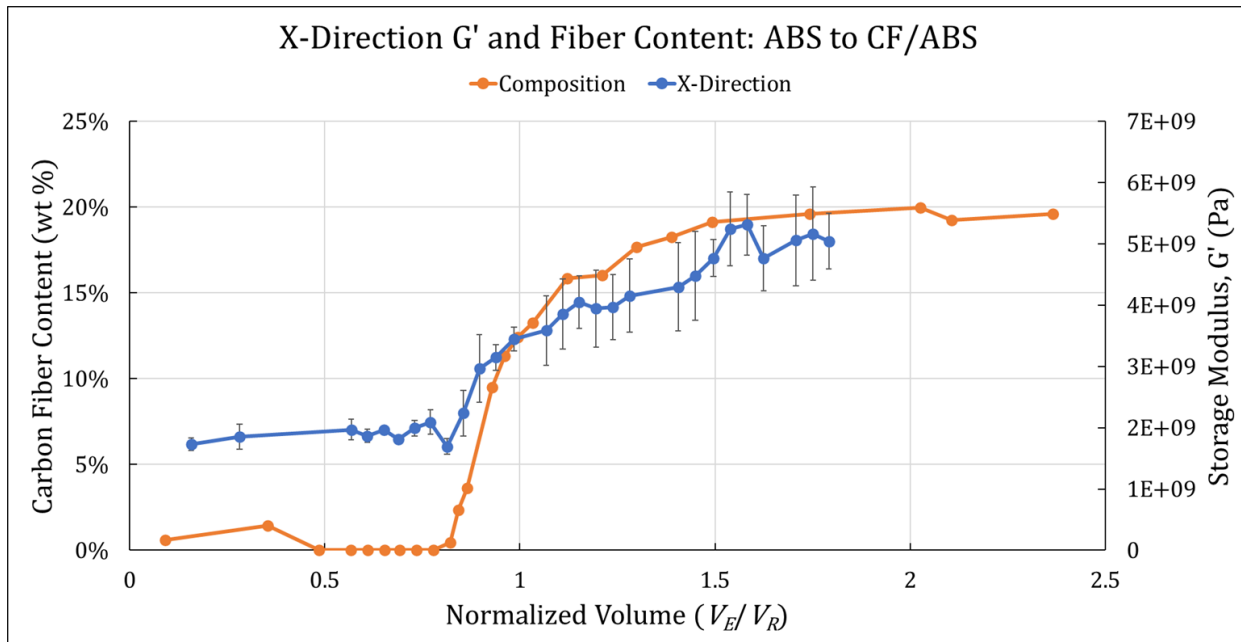


**Figure 5:** Carbon fiber content and storage modulus plotted against the normalized volume for the x-direction samples from the ABS to CF transition directions.

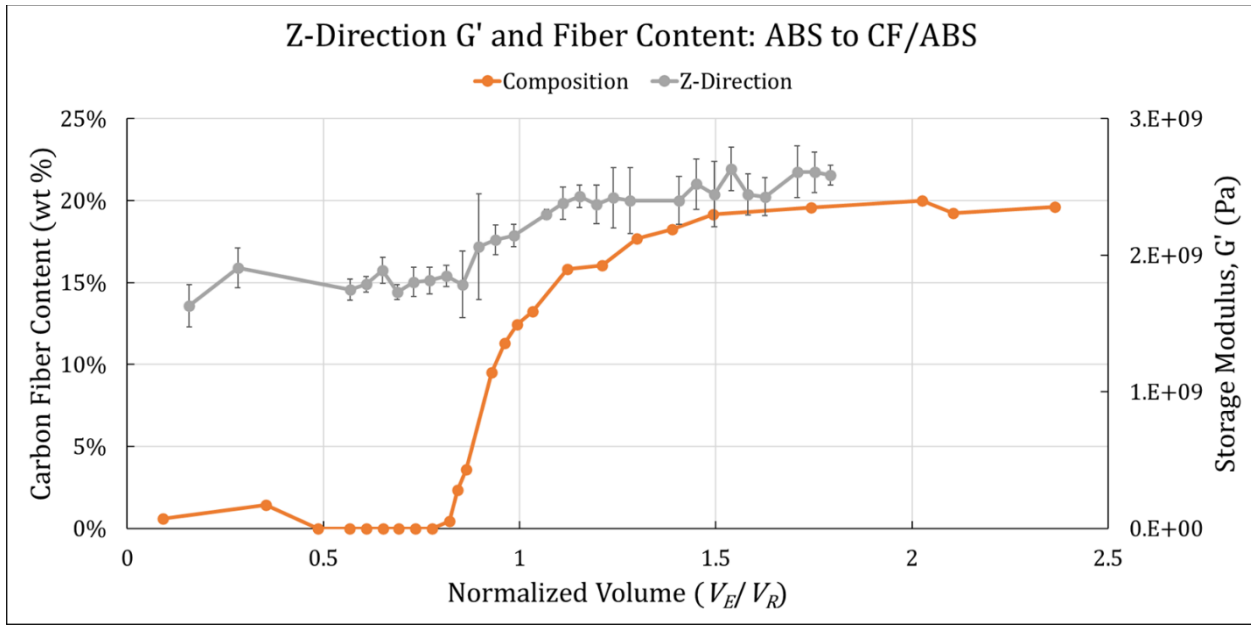


**Figure 6:** Carbon fiber content and storage modulus plotted against the normalized volume for the z-direction samples from the ABS to CF transition directions.

### 3.3 X- vs Z-direction

Figure 7 combines the storage modulus data from Figures 5 and 6. As discussed, the calculated  $G'$  values change with material composition and standard deviation increases with wt % CF regardless of sample orientation. However, the x-direction behavior sees a significant increase in  $G'$  in the CF/ABS region compared to z-direction despite showing similar values while still in the ABS purge zone. One possible cause for this behavior could be limited layer-to-layer bonding due to the presence of carbon fibers near the surface of printed beads, which would clearly not be an issue in the fiber-free ABS. Another source could be the preferential alignment of carbon fibers during deposition increasing performance in the x-direction [23]. Considering this behavior, the effects of the material transition are best seen through analysis of samples oriented in the x-direction.

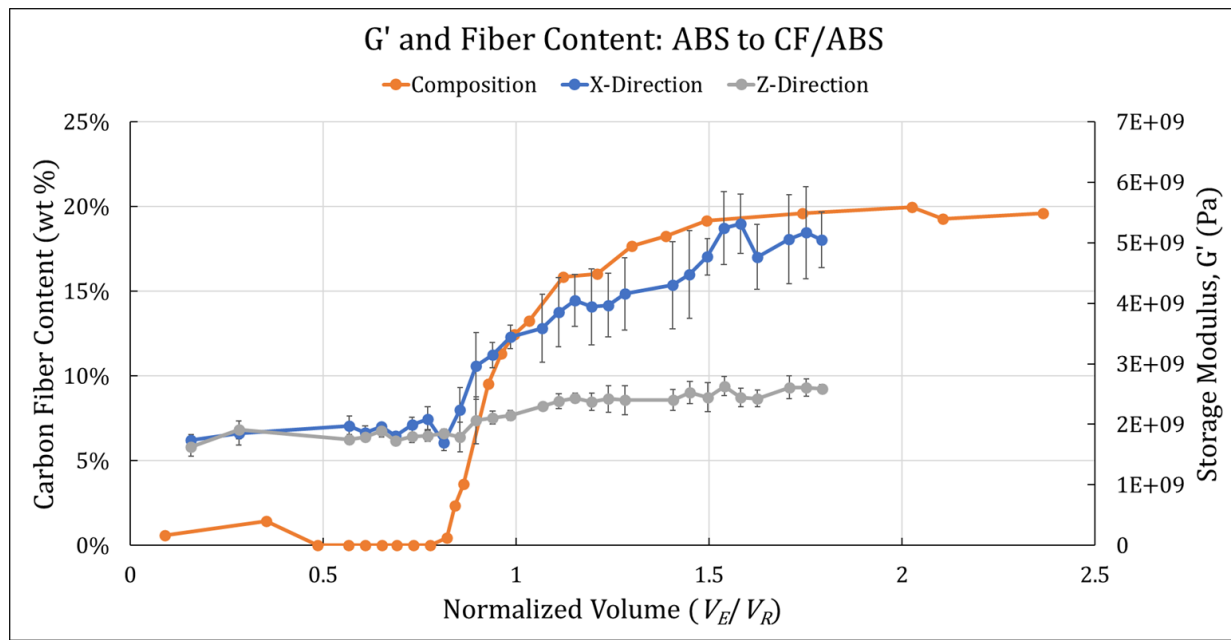


**Figure 7:** Material composition compared to both x- and z-direction samples from the ABS to CF transition direction plotted against normalized volume.

### 3.4 Effect of Transition Direction

The direction of material transition was expected to have minimal, if any, impact on mechanical behavior, so Figure 8 shows the composition variation for the x-direction samples for the CF to ABS transition. Like for the ABS to CF direction,  $G'$  shows a direct and immediate relationship to wt % CF for the CF to ABS transition direction. As carbon fiber content decreases,  $G'$  follows suit, creating both expected plateaus and the continuously changing transition region. Similarly, standard deviation was dependent on fiber content, decreasing as carbon fiber content decreases throughout the material transition. Once again, standard deviation also exhibited relative spikes at the beginning and end of the material transition, which can again be attributed to inadequate mixing of the differently shaped feedstocks. Continuing to follow trends observed in the opposite transition direction, the transition zone was concentrated near  $1 V_N$ . The only noticeable difference in behavior is a slight increase in standard deviation in the ABS region, which is most likely caused by residual carbon fiber stuck on geometry features of the mixing screw design. It is also worth noting that a few data points during the transition zone suffered from a lack of testable samples and did not have a reportable standard deviation, but they were included as they matched the observed and expected trends.

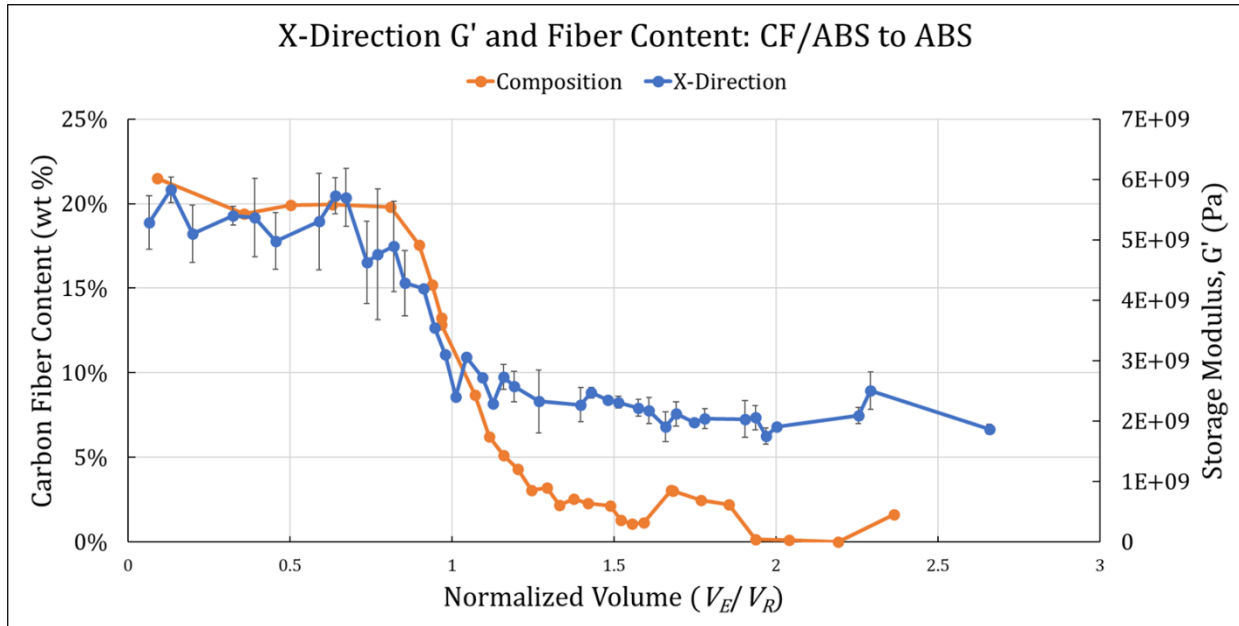


**Figure 8:** CF to ABS material composition and storage moduli for the z-direction samples.

#### 4. Conclusions

Extensive three-point bend DMA testing was conducted on multi-material specimens printed with BAAM and the dual-hopper attachment, and both transition directions were analyzed through determination of  $G'$  for x- and z-direction samples.  $G'$  was plotted with previously determined carbon fiber content against the normalized extruded volume to compare changes in mechanical behavior to changes in material composition. For the studied materials, storage modulus exhibited a clear dependence on material composition regardless of sample orientation. However, x-direction samples experienced a significant change in  $G'$  compared to z-direction specimens, indicating that the effects of the material transition are more apparent for testing of samples oriented in the print direction, which is most likely due to differences in fiber orientation, alignment, and layer-to-layer bonding. Rather than suffering from decreased performance from poor mixing or having to overcome composition thresholds, the multi-material transition zone was characterized by intermediate  $G'$  values, supporting the usage of a transition zone as a replacement for failure-prone discrete boundaries. Furthermore, consistent behavior could enable the deliberate placement of mixed compositions within printed structures for site-specific properties while also reducing material waste associated with switching materials outside the printed structure. In addition to increasing the average  $G'$ , an increase in wt % CF led to an increase in standard deviation. Although the standard deviation in  $G'$  was primarily dependent upon carbon fiber content, it also spiked at the onset and completion of the transition zone relative to surrounding data points. This was attributed to non-uniform mixing when there is a large discrepancy in feedstock percentages. As expected, these observations held true for the opposite transition direction, confirming that transition direction plays a minimal role in mechanical behavior.

Characterization of tensile properties provides an opportunity to further investigate the mechanical properties of the printed material transition region and confirm material composition is the driving force in determining performance. However, there are also opportunities to reduce

the observed standard deviation through improvements in mixing of the pelletized feedstock during extrusion.

### Acknowledgements

Research sponsored by the U.S. Department of Energy, Office of Energy Efficiency and Renewable Energy, Advanced Manufacturing Office, under contract DE-AC05-00OR22725 with UT-Battelle, LLC. The authors would also like to acknowledge funding from the State of Tennessee and Tennessee Higher Education Commission (THEC) through their support of the Center for Materials Processing. Research supported by the National Science Foundation under Award No. 2055529. Thanks to Cincinnati Incorporated and Techmer PM for provided material and equipment. Further thanks to the UTK MABE Maker Lab.

### References

- [1] J. Jiang, A novel fabrication strategy for additive manufacturing processes, Journal of Cleaner Production 272 (2020) 122916.  
<https://doi.org/https://doi.org/10.1016/j.jclepro.2020.122916>.
- [2] J. Jiang, X. Xu, J. Stringer, Support structures for additive manufacturing: A review, Journal of Manufacturing and Materials Processing 2 (4) (2018) 64 Available:  
<https://www.mdpi.com/2504-4494/2/4/64> 2504-4494.
- [3] S. Brischetto, C. Ferro, R. Torre, P. Maggiore, 3d fdm production and mechanical behavior of polymeric sandwich specimens embedding classical and honeycomb cores, Curved and Layered Structures 5 (2018) 80-94. <https://doi.org/10.1515/cls-2018-0007>.
- [4] N. W. Bartlett *et al.*, A 3d-printed, functionally graded soft robot powered by combustion, Science 349 (6244) (2015) 161-165. <https://doi.org/10.1126/science.aab0129>.
- [5] I. Vu, L. Bass, N. Meisel, B. Orler, C. B. Williams, D. A. Dillard, Characterization of multi-material interfaces in polyjet additive manufacturing, Solid Freeform Fabrication Symposium, Austin, TX, (2015). Available:  
<http://utw10945.utweb.utexas.edu/sites/default/files/2015/2015-79-Vu.pdf>
- [6] I. Q. Vu, L. B. Bass, C. B. Williams, D. A. Dillard, Characterizing the effect of print orientation on interface integrity of multi-material jetting additive manufacturing, Addit. Manuf. 22 (2018) 447-461. <https://doi.org/https://doi.org/10.1016/j.addma.2018.05.036>.
- [7] B. Ezair, G. Elber, Fabricating functionally graded material objects using trimmed trivariate volumetric representations, Fabrication and Sculpting Event(2017)
- [8] T. Smith *et al.*, Dual material system for polymer large scale additive manufacturing, Society for the Advancement of Material and Process Engineering 2020, Seattle, WA (2020).
- [9] M. Vaezi, S. Chianrabutra, B. Mellor, S. Yang, Multiple material additive manufacturing – part 1: A review, Virtual & Physical Prototyping 8 (1) (2013) 19-50.  
<https://doi.org/10.1080/17452759.2013.778175>.
- [10] H. Kim, E. Park, S. Kim, B. Park, N. Kim, S. Lee, Experimental study on mechanical properties of single- and dual-material 3d printed products, Procedia Manufacturing 10 (2017) 887-897. <https://doi.org/https://doi.org/10.1016/j.promfg.2017.07.076>.
- [11] F. Roger, P. Krawczak, 3d-printing of thermoplastic structures by fdm using heterogeneous infill and multi-materials: An integrated design-advanced manufacturing approach for factories of the future. 2015.

- [12] N. A. Lee, R. E. Weber, J. H. Kennedy, J. J. Van Zak, M. Smith, J. Duro-Royo, N. Oxman, Sequential multimaterial additive manufacturing of functionally graded biopolymer composites, *3d Print Addit Manuf* 7 (5) (2020) 205-215.  
<https://doi.org/10.1089/3dp.2020.0171>.
- [13] M. J. Mirzaali *et al.*, Mechanics of bioinspired functionally graded soft-hard composites made by multi-material 3d printing, *Composite Structures* 237 (2020) 111867.  
<https://doi.org/https://doi.org/10.1016/j.compstruct.2020.111867>.
- [14] N. Kladovasilakis, K. Tsongas, D. Tzetzis, Finite element analysis of orthopedic hip implant with functionally graded bioinspired lattice structures, *Biomimetics* 5 (3) (2020) 16.  
<https://doi.org/10.3390/biomimetics5030044>.
- [15] P. Heinl, L. Muller, C. Korner, R. F. Singer, F. A. Muller, Cellular ti-6al-4v structures with interconnected macro porosity for bone implants fabricated by selective electron beam melting, *Acta Biomater.* 4 (5) (2008) 1536-1544.  
<https://doi.org/10.1016/j.actbio.2008.03.013>.
- [16] A. Bandyopadhyay, B. Heer, Additive manufacturing of multi-material structures, *Materials Science and Engineering: R: Reports* 129 (2018) 1-16.  
<https://doi.org/https://doi.org/10.1016/j.mser.2018.04.001>.
- [17] M. Naebe, K. Shirvanimoghaddam, Functionally graded materials: A review of fabrication and properties, *Appl. Mater. Today* 5 (2016) 223-245.  
<https://doi.org/10.1016/j.apmt.2016.10.001>.
- [18] R. M. Mahamood, E. T. Akinlabi, Types of functionally graded materials and their areas of application, in: Functionally graded materials. Cham: Springer International Publishing, 2017, pp. 9-21.
- [19] J. Brackett *et al.*, Development of functionally graded material capabilities in large-scale extrusion deposition additive manufacturing, *Solid Freeform Fabrication Symposium*, Austin, TX, (2019). Available:  
<http://utw10945.utweb.utexas.edu/sites/default/files/2019/149%20Development%20of%20Functionally%20Graded%20Material%20Capabi.pdf>
- [20] J. Brackett *et al.*, Characterizing material transitions in large-scale additive manufacturing, *Addit. Manuf.* 38 (2021) 101750.  
<https://doi.org/https://doi.org/10.1016/j.addma.2020.101750>.
- [21] J. Brackett, D. Cauthen, T. Smith, V. Kunc, C. Duty, The influence of processing parameters on the transition zone for blended material 3d printing, *SAMPE 2020 Virtual Series | Additive Manufacturing*, Seattle, WA (2020). Available:  
<https://www.nasampe.org/store/viewproduct.aspx?id=16279755>.
- [22] ASTM Standard D5023-15, Standard test method for plastics: Dynamic mechanical properties: In flexure (three-point bending), ASTM International, West Conshohocken, PA, 2015. <https://doi.org/10.1520/D5023-15>.
- [23] H. L. Tekinalp *et al.*, Highly oriented carbon fiber–polymer composites via additive manufacturing, *Composites Science and Technology* 105 (2014) 144-150.  
<https://doi.org/https://doi.org/10.1016/j.compscitech.2014.10.009>.